Mechatronics 75 (2021) 102541

Contents lists available at ScienceDirect

Mechatronics

journal homepage: www.elsevier.com/locate/mechatronics

Serial-kinematic monolithic nanopositioner with in-plane bender actuators ☆

Steven I. Moore *, Yuen K. Yong, Meysam Omidbeike, Andrew J. Fleming

School of Electrical Engineering and Computing, University of Newcastle, Australia

ARTICLE INFO

Keywords:
Nanopositioning
Atomic force microscopy
Piezoelectric actuators

ABSTRACT

This article describes a monolithic nanopositioner constructed from in-plane bending actuators which provide greater deflection than previously reported extension actuators, at the expense of stiffness and resonance frequency. The proposed actuators are demonstrated by constructing an XY nanopositioning stage with a serial kinematic design. Analytical modeling and finite-element-analysis accurately predicts the experimental performance of the nanopositioner. A 10 μm range is achieved in the X and Y axes with an applied voltage of +/-200 V. The first resonance mode occurs at 250 Hz in the Z axis. The stage is demonstrated for atomic force microscopy imaging.

1. Introduction

Nanopositioning devices are a class of short-range motion stages with resolution on the nanometer scale or below [1]. Applications include atomic force microscopy [2–8], data storage [9], nanofabrication [10,11], cell surgery [12], and precision optics [13].

Piezoelectric tube scanners were the first common nanopositioning systems used in Atomic Force Microscopy (AFM) [14]. Since these are constructed from a single piece of piezoelectric ceramic, they are known as monolithic structures which provide both actuation and some motion guidance [15,16]. The travel range of piezoelectric tubes is determined by the length, radius, and tube wall thickness. They tend to be long (e.g. 50 mm) and thin (e.g. 7 mm diameter) which can be difficult to integrate due the significant vertical height. There is significant scope to explore other monolithic geometries that are similar in cost but provide improved performance and alternative dimensions.

The most common class of nanopositioners are flexure-based devices [17–25]. In these designs, metal flexures guide a central stage which is driven by piezoelectric stack actuators. Metal flexure-based nanopositioners provide the highest performance metrics with respect to displacement gain, resonance frequency, cross-coupling, and load size. However, they are also much larger, heavier, and more costly than monolithic devices like piezoelectric tubes. In addition, assembling and preloading piezoelectric stack actuators are required to avoid damage to the stack actuators [26]. Preload mechanisms require careful design considerations and precise machining which increase manufacturing time and cost.

There is significant demand for low profile positioning systems in applications such as optical microscopy [27], atomic force microscopy [28], and in particular, scanning electron microscopy (SPM) where the load-lock area is typically less than 10 mm in height [29,30]. Products designed for these applications include the SuperFlat AFM from Kleindiek nanotechik [28], the P-541 and P-542 Series from Physik Instrumente [31], and the Nano-Bio and Nano-LPS Series from Mad City Labs [27].

This work combines monolithic and flexure-based design approaches which results in a vertical thickness of less than 1 mm, which is an order of magnitude less than current metal flexure based devices. The advantages of the proposed approach over metal flexure designs are generalized by lower vertical height; lower mass; no preload mechanism; compatibility with vacuum and low temperature applications. The proposed method is light weight, which makes it suitable for applications such as camera stabilization and optical scanning from small-scale air vehicles [32]. The simple mechanical structure of the proposed method also avoids the need for stack actuators and the resulting preloading requirements. Since bonding or encapsulation materials are not required, the reported monolithic design can also be easily adapted to high-vacuum and cryogenic applications.

The disadvantages of the proposed method stem from the low vertical height that results in low vertical stiffness. This results in higher vertical cross-coupling and a lower payload capability compared to metal flexure devices. The most useful range of payload masses for the proposed method is less than 10 g.

Microelectromechanical systems (MEMs) are another class of monolithic flexure-based nanopositioners [33]. These devices provide the

☆ This paper was recommended for publication by Associate Editor Robert T. M'Closkey.

* Corresponding author.
E-mail addresses: steven.i.moore@uon.edu.au (S.I. Moore), meysam.omidbeike@uon.edu.au (M. Omidbeike).
URL: http://www.precisionmechatronicslab.com (A.J. Fleming).

https://doi.org/10.1016/j.mechatronics.2021.102541
Received 24 April 2020; Received in revised form 15 February 2021; Accepted 7 March 2021
Available online 23 March 2021

Table 1
A comparison of monolithic extension actuators [41] and the in-plane bending actuators described in this work. L is the beam length, t_y is the width see Fig. 3, and $\propto$ means proportional to.

	Actuator type	
	Extension [41]	In-plane bender
Deflection	$\propto L$	$\propto L^2/t_y$
In-plane stiffness	$\propto t_y/L$	$\propto t_y/L^2$
Out-of-plane stiffness	Similar	Similar
Best suited to	Parallel kinematic	Serial kinematic

smallest size and the opportunity to integrate sensing mechanisms [33–35]. MEMs based nanopositioners are best suited to payload masses in the milligram range. The proposed methods represent an intermediate point between MEMs based nanopositioners and metal-flexure based nanopositioners.

1.1. Contribution

This article describes a new actuation method for monolithic nanopositioners using in-plane bending actuators. As illustrated in Figs. 1 and 2, each actuator is made from a thin piezoelectric beam with four top electrodes and a grounded bottom electrode. When opposite voltages are applied to the top electrodes, the resultant deflection is shown in Fig. 3. A unique feature of this design is that the moving end deflects in a plane and does not rotate. Compared to a piezoelectric bimorph bender, the motion is lateral rather than vertical [36].

The methods described herein are compared to previous and future work in Fig. 1, including the previous beam extension actuators (top), the topic of this work (middle), and future work (bottom). Other related work has also included closed-loop [37] and feedforward [38] control of extension actuators. Future work (bottom) aims at extending the monolithic concept to a bimorph structure which enables vertical and angular motion [39,40].

A summary of the application characteristics of extension [41] and in-plane bending actuators are listed in Table 1. In-plane bending actuators provide increased flexibility in the choice of travel range since the deflection is proportional to the actuator length squared, rather than directly proportional [41]. The beam width of an in-plane bending actuator can be used to control the trade-off between stiffness and travel range. In practice, reduced in-plane stiffness is not expected to be a significant disadvantage since the operating speed is limited by the first resonance mode, which is an out-of-plane mode primarily determined by the material thickness and is similar for both approaches.

A preliminary version of this work was presented at the IEEE International Conference on Advanced Intelligent Mechatronics in 2018 [42] which used Euler–Bernoulli beam theory to estimate the static deflection of each bender, and a lumped mass and stiffness approach to estimate the combined deflection and stiffness. This modeling approach does not capture the out-of-plane dynamics which are the lowest frequency and most significant eigenmodes of the system.

Compared to [42], the present work uses a combination of Euler–Bernoulli beam theory and Hamilton's principle to predict the total deflection in each axis and the first resonance modes in both the lateral and vertical directions. This work also extends on [42] with an experimental measurement of resonance modes, measurement of the cross-coupling between axes, and application to atomic force microscopy imaging.

In the remainder of the article, Section 2 outlines the structural design, fabrication, and actuating principles of the nanopositioner. Sections 3 and 4 present a reduced-order model of an active flexure from which the dynamics of the nanopositioner are predicted. Section 5 presents finite element analysis (FEA) of the device which validates the modeling of the nanopositioner. Section 6 presents the experimental performance of the device which examines the range, cross-coupling, non-linearity, and modal characteristics. Section 7 demonstrates the use of the nanopositioner for atomic force microscopy.

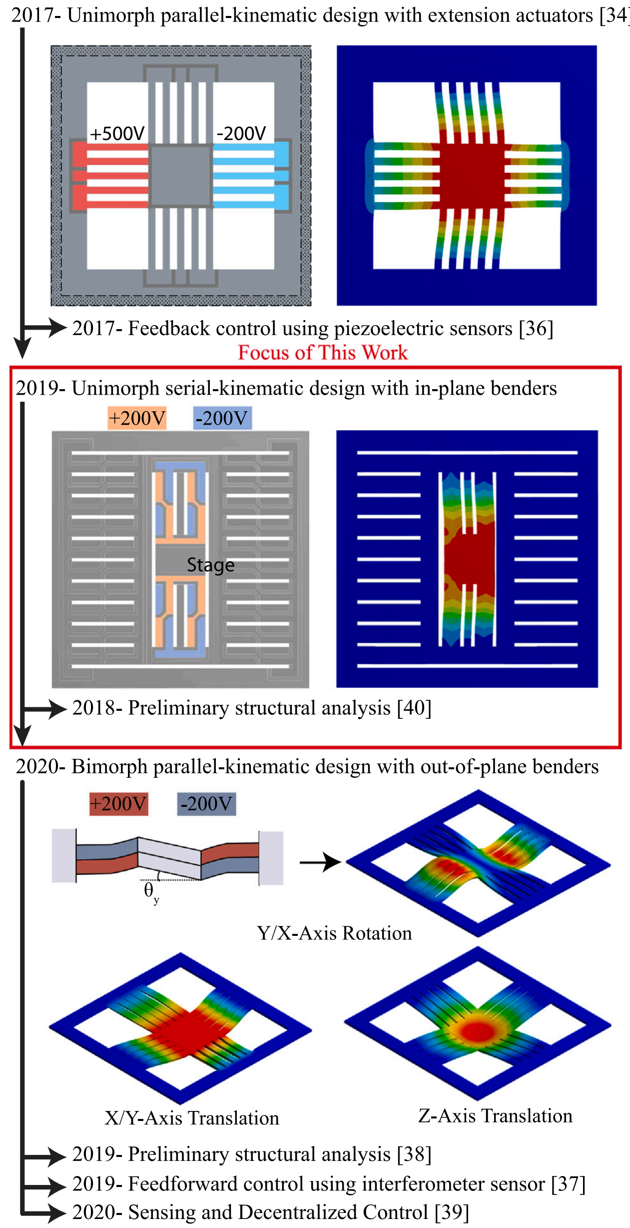

Fig. 1. The contribution of this article in relation to other work on monolithic nanopositioning systems is shown in the red box. (For interpretation of the references to color in this figure legend, the reader is referred to the web version of this article.)

2. Design and fabrication

Fig. 2(a) shows the fabricated serial-kinematic nanopositioner where a smaller inner stage is nested into a larger outer stage. The nanopositioner is fabricated from a single square sheet of PZT-5 A ceramic of thickness 500 μm. The piezoelectric sheet is coated with a 5 μm layer of nickel on both sides. The mechanical and electrode features are created by ultrasonic machining. Fig. 2(b) shows the mechanical features and the nickel electrode arrangement with dimensions. The nickel layer on the reverse side is not etched.

The dimensions in Fig. 2 were chosen using the analysis and simulation methods described in the following sections to provide a 10 μm

(a) The machined piezoelectric sheet forming the nanopositioner.

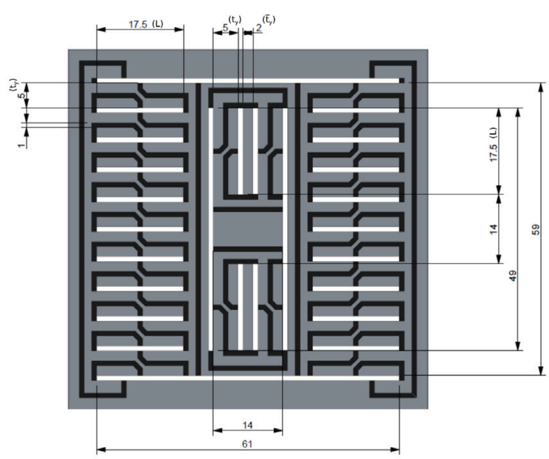

(b) The dimensions of the nanopositioner. Cutouts are shown in white, the nickel coating is shown in grey and the PZT-5A is shown in black. Units are in mm.

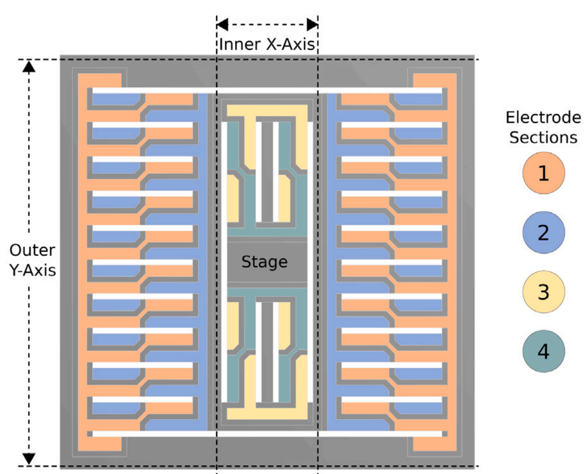

(c) The electrode sections of the nanopositioner for translation in the X and Y axes.

Fig. 2. The nanopositioner design. (a) The photo of the prototype design. (b) Schematic with the structural dimensions. (c) Schematic of the piezoelectric electrode layout.

range in the X and Y-axis, which is suitable for AFM imaging. The piezo sheet (72.4 mm × 72.4 mm) is identical to earlier work [41], which

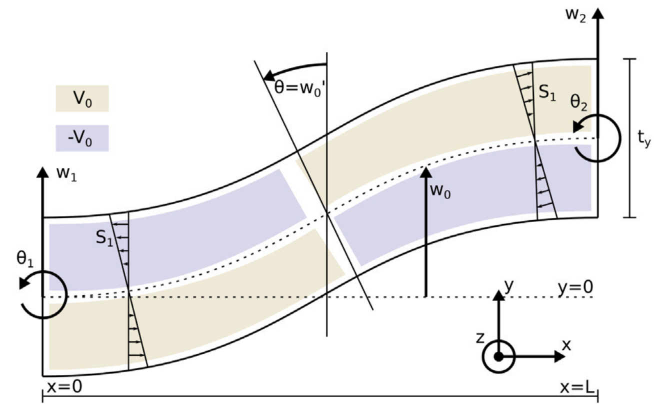

Fig. 3. Each active flexure has four electrodes, one on each quarter of the flexure in the X–Y plane. Two of the electrodes are actuated positively and the other two are actuated negatively. The diagram shows the positive orientation of the deflection $w_0(x)$, rotation $w_0'(x)$, and the four degrees-of-freedom $(w_1, \theta_1, w_2, \theta_2)$ of the reduced order model.

allows a direct performance comparison. The number of flexures were chosen to maximize the stiffness given the available space. The number of parallel flexures does not affect the travel range, but the number is proportional to stiffness, so the number should be maximized. The other trade-offs between the dimensions and performance are summarized in Table 1.

The motion of the X and Y axes are constrained by a set of thick flexures on either side of the stage. The flexures guide the nanopositioner in the compliant directions, and provide the mechanism for actuation. The inner X axis is guided by four active flexures and two non-active flexures. The outer Y axis is guided by 20 active flexures.

The electrode over each active flexure is split into four quadrants as shown in Fig. 3. Diagonally opposite quadrants are electrically connected. With the bottom electrode grounded, opposite voltages are applied to the two electrode sections to create side-to-side motions. When actuators of a single axis are moved in the same direction, translational motions are generated. When they are moved in opposing directions, rotational motion is generated. The electrode arrangement of the complete nanopositioner is shown in Fig. 2(c). The electrode sections on each axis are driven with opposite polarity voltages, where Sections 1 and 2 develop motion in the Y axis and Sections 3 and 4 develop motion in the X axis.

The nanopositioner is mounted onto a metal frame, as shown in Fig. 2(a), with the grounded electrode facing upward. This prevents access to the high voltage electrodes on the opposite side for the safety of the user and protection of the sample and equipment interacting with the device.

3. Electromechanical model of an active flexure

To analyze the dynamics of the piezoelectric nanopositioner, a model of a single piezoelectric flexure, shown in Fig. 3, is derived. The constitutive equations of the piezoelectric material, Euler–Bernoulli beam theory, and Hamilton's principle are applied to relates the stress, strain, electric field, and electric displacement in the structure. This results in a voltage-deflection model of the active flexure.

3.1. Stress–displacement relationship

Euler–Bernoulli beam theory parameterizes the 3-dimensional displacement field in the structure in terms of the 1-dimensional deflection of the flexure w_0 [43–45],

$$u_1(x, y, z) = -y w_0'(x), \tag{1}$$

$$u_2(x,y,z) = w_0(x), \tag{2}$$

$$u_3(x,y,z) = 0, \tag{3}$$

where (u_1, u_2, u_3) is the displacement of an infinitesimal piece of the flexure in the X, Y, and Z axes respectively, and the prime ($'$) is the derivative with respect to x. w_0' is the angle of rotation of the flexure around the neutral axis as shown in Fig. 3. The displacement field indicates that: the displacement in the Y axis is solely due to the deflection of the flexure; there is no displacement in the Z axis; and displacement in the X axis is due to the cross-sectional rotation of the flexure. With the above displacement field, there is only one non-zero component of the strain, that is,

$$S_1(x,y,z) = u_1' = -y w_0''. \tag{4}$$

3.2. Electric field–voltage relationship

A parallel-plate capacitive structure is used to model the generated electric field. One-side of the flexure is grounded, and the other is split into four electrodes distributed in the XY-plane. The piezoelectric flexure is polarized along the Z axis. The electric field is,

$$E_3(x,y,z) = -B_e(x,y)V_e \tag{5}$$

where V_e is the magnitude of the input voltage and B_e models the geometry of the electrodes,

$$B_e(x,y) = \frac{1}{t_z}\begin{cases} -1 & x < L/2,\ y > 0 \\ 1 & x < L/2,\ y < 0 \\ 1 & x > L/2,\ y > 0 \\ -1 & x > L/2,\ y < 0 \end{cases}, \tag{6}$$

where t_z is the thickness of the flexure in the Z direction.

3.3. Constitutive equations

An Euler–Bernoulli beam has only one non-zero stress and strain component, and the electric field is only applied in the polarization direction of the piezoelectric material. In this case, the constitutive equations simplify to

$$T_1 = c_{11}S_1 - e_{31}E_3, \tag{7}$$

$$D_3 = e_{31}S_1 + \varepsilon_{33}E_3, \tag{8}$$

where T_1 is the stress, D_3 is the electric displacement, c_{11} is Young's modulus, e_{31} is the piezoelectric coefficient, and ε_{33} is the permittivity.

3.4. Discretization of the model

To simplify the model, deflections of the flexure are parameterized by four degrees-of-freedom (DOFs), which are the deflections (w_1, w_2) and rotations (θ_1, θ_2) at both ends of the flexure as shown in Fig. 3. To form the reduced-order model of the flexure, the deflection is expressed as

$$w_0(x) = N_e(x)d_e, \tag{9}$$

where N_e is a vector of interpolation functions and d_e is a vector of the DOFs,

$$d_e = \begin{bmatrix} w_1 & \theta_1 & w_2 & \theta_2 \end{bmatrix}^T. \tag{10}$$

The interpolation functions are the Hermite cubic splines given by [46],

$$N_e(x) = \begin{bmatrix} N_1(x) & N_2(x) & N_3(x) & N_4(x) \end{bmatrix}, \tag{11}$$

where,

$$N_1(x) = 1 - \tfrac{3x^2}{L^2} + \tfrac{2x^3}{L^3}, \tag{12}$$

$$N_2(x) = L\left(\tfrac{x}{L} - \tfrac{2x^2}{L^2} + \tfrac{x^3}{L^3}\right), \tag{13}$$

$$N_3(x) = \tfrac{3x^2}{L^2} - \tfrac{2x^3}{L^3}, \tag{14}$$

$$N_4(x) = L\left(-\tfrac{x^2}{L^2} + \tfrac{x^3}{L^3}\right). \tag{15}$$

For the development of the model, the strain S_1 is expressed in terms of d_e by substituting Eq. (9) into Eq. (4), which gives,

$$S_1 = -yN_e''(x)d_e = B_s(x,y)d_e. \tag{16}$$

3.5. The governing differential equation

Hamilton's principle is the fundamental physical principle used to derive the governing differential equations of the piezoelectric flexure. It is mathematically stated as [44,45,47],

$$0 = \delta \int_{t_1}^{t_2} T - H\, dt, \tag{17}$$

where H is the enthalpy of the piezoelectric flexure, T is the kinetic energy, δ is the variational operator, and (t_1, t_2) is an arbitrary time interval. The expressions for the enthalpy and kinetic energy are,

$$H = \frac{1}{2}\int_\Omega T_1 S_1 - D_3 E_3\, d\Omega, \tag{18}$$

$$T = \frac{1}{2}\int_\Omega \rho\left(\dot{u}_1^2 + \dot{u}_2^2 + \dot{u}_3^2\right)\, d\Omega, \tag{19}$$

where the domain over the volume of the flexure is

$$\Omega = \{(x,y,z) : x \in [0,L],\ y \in [-\tfrac{t_y}{2}, \tfrac{t_y}{2}],\ z \in [0, t_z]\}, \tag{20}$$

and ρ is the material density. The constitutive equation from Eq. (7) and the model discretization from Eqs. (5), (9) and (16) are substituted into the above energy expressions. Note that in Euler–Bernoulli beam theory the rotary inertia is assumed to have a negligible contribution to the kinetic energy and is ignored [48]. In terms of the discretized parameters V_e and d_e, the energy expressions are

$$H = \frac{1}{2}d_e^T K_e d_e + d_e^T P_e V_e - \frac{1}{2}\int_\Omega \varepsilon_{33}(B_e V_e)^2\, d\Omega, \tag{21}$$

$$T = \frac{1}{2}d_e^T M_e d_e, \tag{22}$$

where the parameters M_e, K_e, and P_e are,

$$M_e = \int_\Omega \rho N_e^T N_e\, d\Omega, \tag{23}$$

$$K_e = \int_\Omega c_{11} B_s^T B_s\, d\Omega, \tag{24}$$

$$P_e = \int_\Omega e_{31} B_s^T B_e\, d\Omega. \tag{25}$$

Substituting Eqs. (21) and (22) into Eq. (17) and evaluating Hamilton's principle results in the reduced-order differential equation that governs the dynamics of the piezoelectric flexure,

$$M_e \ddot{d}_e + K_e d_e + P_e V_e = 0. \tag{26}$$

Eqs. (23)–(25) for the mass, stiffness, and piezoelectric matrices of the reduced-order model are evaluated as,

$$M_e = \frac{\rho A L}{420}\begin{bmatrix} 156 & 22L & 54 & -13L \\ 22L & 4L^2 & 13L & -3L^2 \\ 54 & 13L & 156 & -22L \\ -13L & -3L^2 & -22L & 4L^2 \end{bmatrix}, \tag{27}$$

$$K_e = \frac{c_{11} I}{L^3}\begin{bmatrix} 12 & 6L & -12 & 6L \\ 6L & 4L^2 & -6L & 2L^2 \\ -12 & -6L & 12 & -6L \\ 6L & 2L^2 & -6L & 4L^2 \end{bmatrix}, \tag{28}$$

$$P_e = \frac{e_{31} t_y^2}{8L}\begin{bmatrix} -6 & -3L & 6 & -3L \end{bmatrix}^T, \tag{29}$$

where the area A and moment of inertia I are,

$$A = t_z t_y, \tag{30}$$

$$I = \tfrac{t_z t_y^3}{12}. \tag{31}$$

Table 2
Parameters of the piezoelectric flexures for modeling.

Description	Parameter	Value
Flexure length (mm)	L	17.5
In-plane flexure thickness (mm)	t_y	5
In-plane small flexure thickness (mm)	$\bar{t}_y$	2
Out-of-plane flexure thickness (mm)	t_z	0.5
Elastic modulus (GPA)	c_{11}	66
Density (kg/m^3)	ρ	7800
Piezoelectric coefficient (C/m^2)	e_{31}	−10.92
Number of inner stage flexures	n_i	4
Number of small inner stage flexures	$\bar{n}_i$	2
Number of outer stage flexures	n_o	20

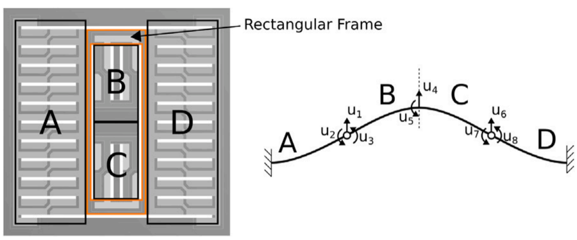

Fig. 4. The out-of-plane motion is modeled by four segments. The rectangular frame that couples the inner and outer axes is modeled as a hinge. The degrees-of-freedom of the reduced-order model are label.

4. Electromechanical model of the piezoelectric nanopositioner

In Section 4.1, the out-of-plane resonance frequencies are derived using a combination of the flexure models from Section 3 with the corresponding thickness and width parameters for bending in the out-of-plane direction. In addition, since there is no actuation in the out-of-plane direction, the piezoelectric constant can be set to zero. Section 4.2 combines a set of piezoelectric flexure models derived in Section 3 with appropriate boundary conditions to derive the in-plane displacement per volt.

4.1. Static modeling

The static deflection of the nanopositioner is derived by assuming the moving platform is rigid and the flexures are constrained with a fixed-guided configuration. The displacement of the inner axis is defined as q_i, and the displacement of the outer axis is q_o. With the fixed-guided configuration of each flexure, the rotations θ_1 and θ_2, and the deflection at the fixed-end w_1 are therefore zero. The displacement at the guided end is equal to either q_i or q_o. As a result, d_e of each flexure is expressed as,

$$d_e = \begin{cases} T_q q_i & \text{for inner axis flexures} \\ T_q q_o & \text{for outer axis flexures} \end{cases}, \tag{32}$$

$$T_q = \begin{bmatrix} 0 & 0 & 1 & 0 \end{bmatrix}^T. \tag{33}$$

Next, the model in Eq. (26) for each flexure is assembled into a single system for each axis. For the inner-axis, the static model is

$$0 = \left(n_i T_q^T K_e T_q + \bar{n}_i T_q^T \bar{K}_e T_q \right) q_i + n_i T_q^T P_e V_i, \tag{34}$$

$$= \frac{12 c_{11} (n_i I + \bar{n}_i \bar{I})}{L^3} q_i + n_i \frac{3 e_{31} t_y^2}{4L} V_i, \tag{35}$$

where n_i is the number of active flexures connected to the stage, and V_i is the inner-axis input voltage. In addition, there are two smaller flexures connected to the inner stage which are passive. Their number, thickness, moment of inertia, and stiffness matrix are designated as $\bar{n}_i$, $\bar{t}_y$, $\bar{I}$, and $\bar{K}_e$ respectively. With the parameters in Table 2 the gain of the inner axis q_i/V_i is calculated to be 14.73 nm V^{-1}, which agrees with the FEA and experimental results summarized in Table 6.

Table 3
The parameters of the reduced order model of the out-of-plane motion.

Description	Parameter	Value
Outer-axis effective length	L_1	17.5 mm
Outer-axis effective width	t_{y1}	50 mm
Inner-axis effective length	L_2	24.5 mm
Inner-axis effective width	t_{y2}	12 mm

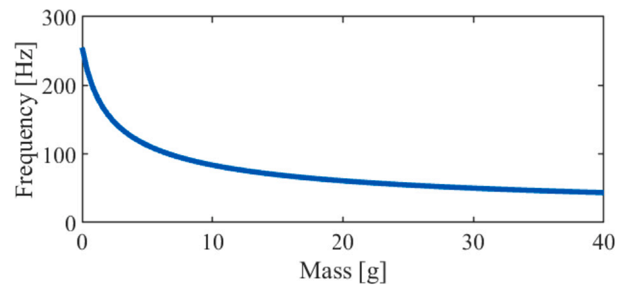

Fig. 5. The change in the first resonance frequency as a point mass is added to the center of the nanopositioner.

For the outer-axis, the static model is,

$$0 = n_o T_q^T K_e T_q q_o + n_o T_q^T P_e V_o \tag{36}$$

$$= n_o \frac{12 c_{11} I}{L^3} q_o + n_o \frac{3 e_{31} t_y^2}{4L} V_o \tag{37}$$

where n_o is the number of flexures connected to the outer-axis, and V_o is the outer-axis input voltage. The gain of the outer-axis with the parameters listed in Table 2 is 15.20 nm V^{-1}, which agrees with the FEA and experimental results summarized in Table 6.

4.2. Dynamic modeling

The first modal frequency of the nanopositioner is an out-of-plane mode. Its frequency is important as it limits the speed at which the nanopositioner can be operated. A reduced-order model is developed to estimate the first out-of-plane resonance frequency. The out-of-plane motion of the serial kinematic stage is modeled by four segments as shown in Fig. 4. The segments are labeled A through to D. Segments A and D model the action of the outer-axis flexures and segments B and C model the action of the inner-axis flexures. The rectangular frame that couples the inner and outer axes is modeled as a hinge to account for its compliant nature. The effective width and length of each segment is listed in Table 3. The effective length of the inner-axis is extended to account for the compliant nature of the inner-axis stage. For out-of-plane motion the moment of inertia is $I = t_z^3 t_y / 12$.

(26) is used to describe each beam segment in the out-of-plane model. The resulting assembled system has eight degree-of-freedom, with the DOFs labeled in Fig. 4. u_1 and u_6 are deflections of the rectangular frame. u_2, u_3, u_7, and u_8 are the rotations at the rectangular frame. The deflection and rotation of the inner-axis stage are defined as u_4 and u_5 respectively. Due to symmetry, kinematic constraints $u_1 = u_6$, $u_2 = -u_8$, $u_3 = -u_7$, and $u_5 = 0$ are defined. The resulting four degree-of-freedom system is,

$$M_z \ddot{u}_z + K_z u_z = 0, \tag{38}$$

where

$$M_z = \begin{bmatrix} \frac{26(A_1 L_1 + A_2 L_2)\rho}{35} & \frac{-11 A_1 L_1^2 \rho}{105} & \frac{11 A_2 L_2^2 \rho}{105} & \frac{9 A_2 L_2 \rho}{35} \\ \frac{-11 A_1 L_1^2 \rho}{105} & \frac{2 A_1 L_1^3 \rho}{105} & 0 & 0 \\ \frac{11 A_2 L_2^2 \rho}{105} & 0 & \frac{2 A_2 L_2^3 \rho}{105} & \frac{13 A_2 L_2^2 \rho}{210} \\ \frac{9 A_2 L_2 \rho}{35} & 0 & \frac{13 A_2 L_2^2 \rho}{210} & \frac{26 A_2 L_2 \rho}{35} \end{bmatrix}, \tag{39}$$

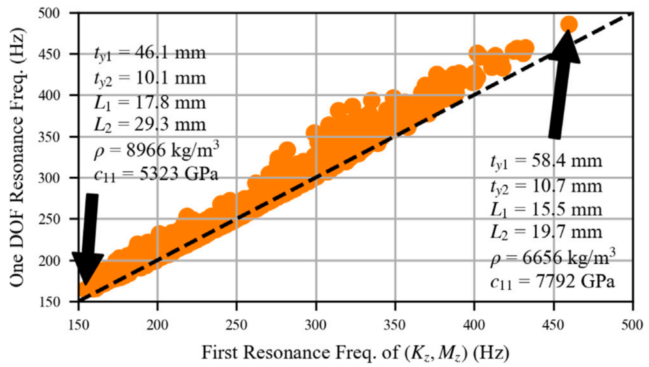

Fig. 6. A comparison of the resonance frequencies predicted by the one and four degree-of-freedom models. 1000 random geometries were considered with up to 20% variation in the model parameters. The one DOF model is observed to overestimate the resonance frequency.

Table 4
Piezoelectric properties for the PZT-5A bimorph sheet from Piezo System Inc.

Piezoelectric coefficient (C/m^2)	e_{31}	e_{33}	e_{15}
	−10.92	12.08	12.29
Relative permittivity	ε_{11}	ε_{33}	
	916	830	

$$K_z = \begin{bmatrix} \frac{24EI_1}{L_1^3}+\frac{24EI_2}{L_2^3} & \frac{-12EI_1}{L_1^2} & \frac{12EI_2}{L_2^2} & \frac{-24EI_2}{L_2^3} \\ \frac{-12EI_1}{L_1^2} & \frac{8EI_1}{L_1} & 0 & 0 \\ \frac{12EI_2}{L_2^2} & 0 & \frac{8EI_2}{L_2} & \frac{-12EI_2}{L_2^2} \\ \frac{-24EI_2}{L_2^3} & 0 & \frac{-12EI_2}{L_2^2} & \frac{24EI_2}{L_2^3} \end{bmatrix}, \tag{40}$$

$$u_z = \begin{bmatrix} u_1 & u_2 & u_3 & u_4 \end{bmatrix}^T, \tag{41}$$

where (L_1, I_1, A_1) are parameters of the outer-axis and (L_2, I_2, A_2) are parameters of the inner-axis. The resonance frequencies of the system in Eq. (38) are evaluated with the eigenvalue problem,

$$\left(K_z - \omega_z^2 M_z\right) U_z = 0, \tag{42}$$

where U_z is the mode shape and ω_z is the resonance frequency. The solution of the eigenvalue problem using the parameters in Table 3 gives a resonance frequency of $\omega_z = 1604.5$ rad s^{-1} $\equiv 255.2$ Hz, which agrees with the FEA and experimental results summarized in Table 6. The mode shape is,

$$U_z = \left[\, 2.006\times10^{-3}\ 1.704\times10^{-1}\ 9.852\times10^{-1}\ 1.733\times10^{-2}\,\right]^T. \tag{43}$$

Masses placed on the nanopositioner reduce the resonance frequency. A point mass at the center of the nanopositioner was added to the four-DOF model and the resulting change in resonance frequency with respect to mass is shown in Fig. 5.

The above four-DOF system is suited for fast numerical design optimization, but does not provide intuitive insight into the direct effects of the design parameters on the resonance frequency. To provide a concise analytical expression relating the design parameters to the first resonance frequency, the motion of the system is parameterized by a single DOF q_z. The DOFs u_z are constrained by the mode shape, that is $u_z = U_z q_z$, and the system in (38) becomes,

$$U_z^T M_z U_z \ddot{q}_z + U_z^T K_z U_z q_z = 0. \tag{44}$$

The resonance frequency of the one DOF system is

$$\omega_z^2 = \frac{U_z^T K_z U_z}{U_z^T M_z U_z}. \tag{45}$$

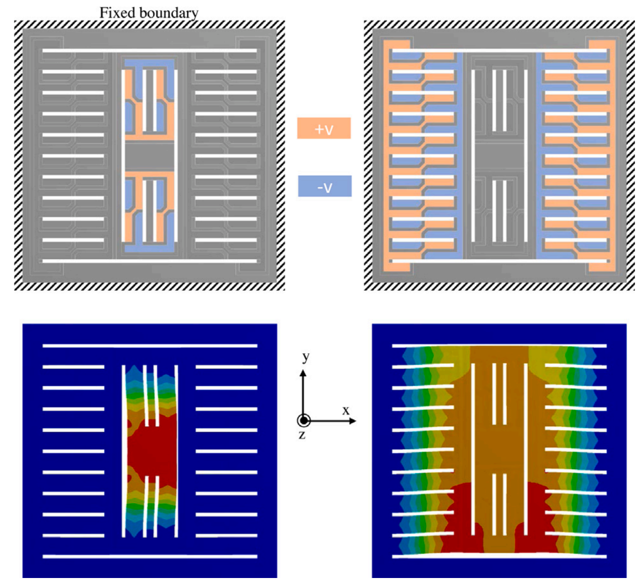

Fig. 7. Simulated displacement along the x and y axes when +1 V is applied to the electrodes in orange and −1 V is applied to the electrodes in blue. (For interpretation of the references to color in this figure legend, the reader is referred to the web version of this article.)

Evaluating (45) with the eigenvector in (43) provides an expression for the first modal frequency, that is

$$\omega_z^2 = \frac{\begin{array}{l} c_{11} I_1 \left[\frac{0.232}{L_1} - \frac{0.0082}{L_1^2} + \frac{9.66\times10^{-5}}{L_1^3}\right] \\ +c_{11} I_2 \left[\frac{7.77}{L_2} - \frac{0.362}{L_2^2} + \frac{0.005\,64}{L_2^3}\right] \end{array}}{\begin{array}{l} \rho A_1 \left[5.53\times10^{-4} L_1^3 - 7.16\times10^{-5} L_1^2 + 2.99\times10^{-6} L_1\right] \\ +\rho A_2 \left[0.0185 L_2^3 + 0.002\,53 L_2^2 + 2.44\times10^{-4} L_2\right] \end{array}}. \tag{46}$$

To assess the validity of the above simplification, 1000 random mechanical systems were compared with up to 20% variation of the model parameters. The resonance frequencies predicted by both methods are plotted in Fig. 6. The one-DOF approximation is observed to overestimate the resonance frequency. However, the accuracy is considered to be acceptable for the purposes of design optimization.

For the chosen stage geometry, the analytical resonance frequencies are 8321 Hz in the X-axis, and 8986 Hz in the Y-axis, which are compared to the FEA and experimental results in Table 6. The analytical values are higher than the measured resonance frequencies; however, this was expected due to the required simplifications. It should be noted that the lateral resonance modes have a negligible effect on performance since they occur at much higher frequencies than the vertical resonance modes. That is, in the majority of applications, the vertical resonance mode will be the limiting factor.

5. Finite-element modeling

A numerical finite-element-analysis (FEA) model of the monolithic stage was constructed using ANSYS workbench. The displacement of all four edges are fixed as shown in Fig. 7. The piezoelectric properties of the stage are modeled using the ANSYS Piezo and MEMS Application Customization Toolkit (ACT) extension. The piezoelectric properties for PZT-5 A are listed in Table 4. Each piezoelectric layer is polarized outwards along its thickness direction.

To obtain the displacement per unit voltage along the X and Y axes, +1 V and −1 V is applied to the electrodes in orange and blue respectively as shown in Fig. 7. The corresponding displacement is shown in the same figure. The static gain of the inner x-axis and outer

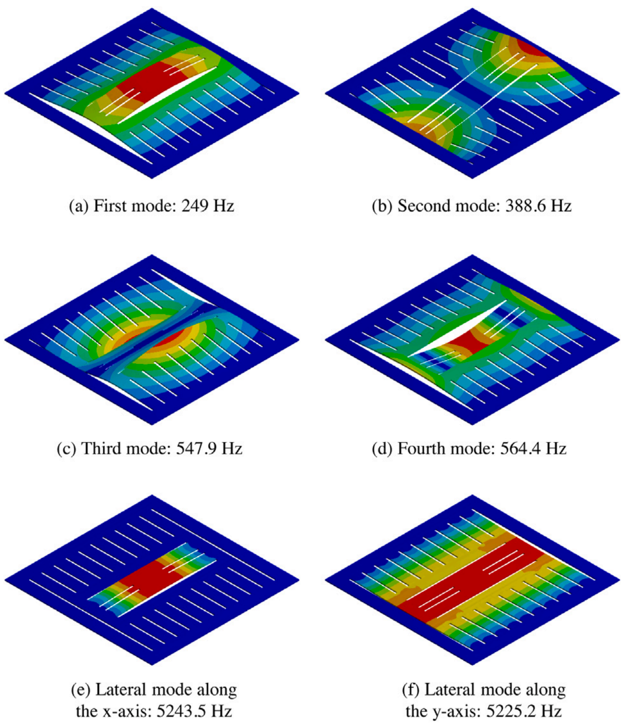

Fig. 8. Simulated resonance frequencies of the serial-kinematic planar stage. The displacements are normalized and exaggerated for display purposes.

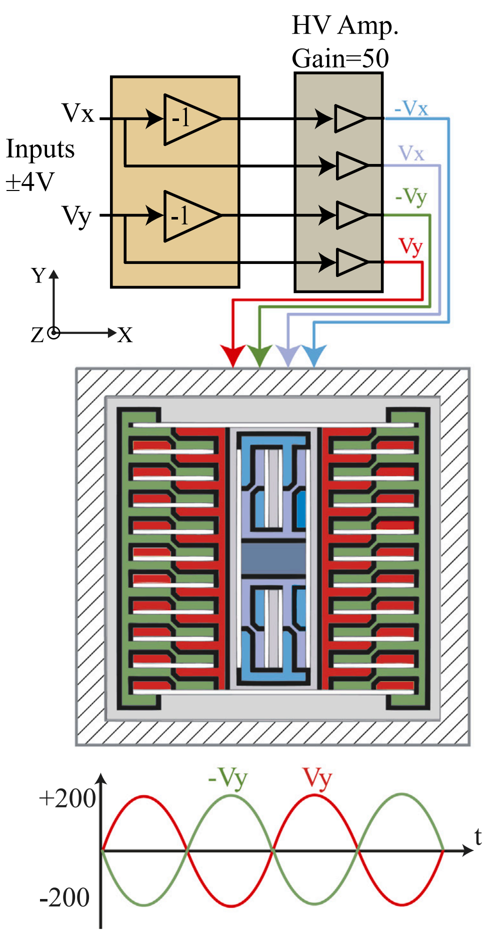

Fig. 9. The nanopositioner is driven by a high-voltage amplifier that provides the required voltages to the four sets of electrodes for in-plane actuation.

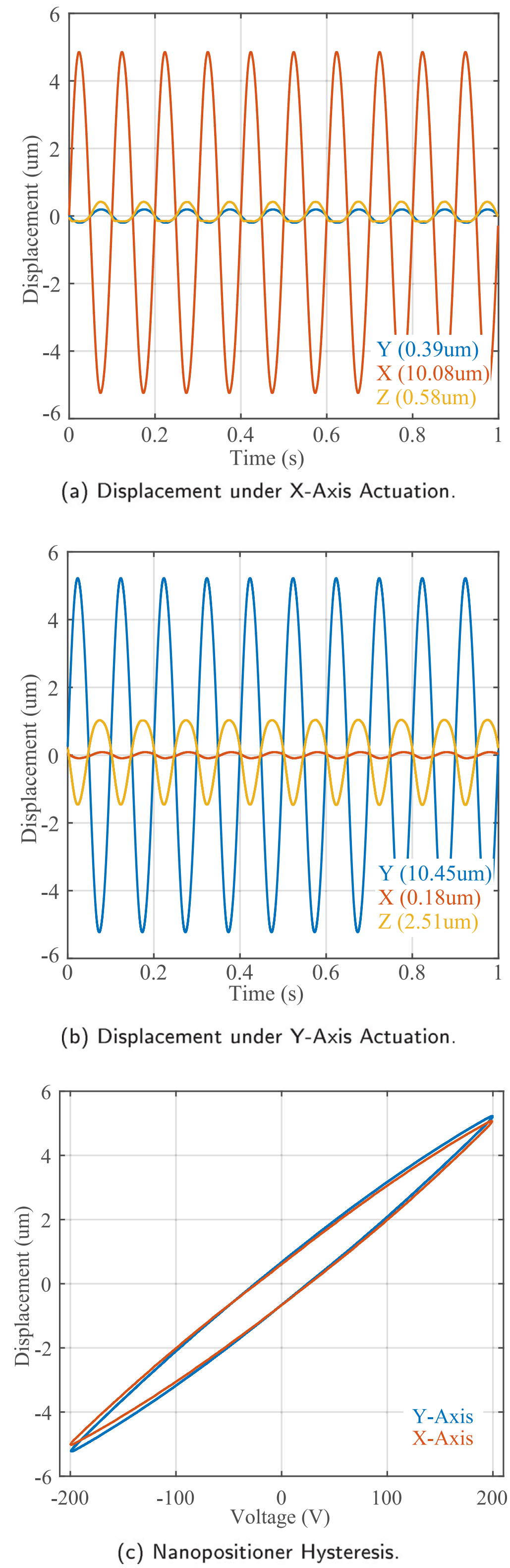

Fig. 10. The displacement of the nanopositioner.

y-axis is 18.6 nm/V and 18.1 nm/V respectively, which agree with the experimental results summarized in Table 6.

The resonance frequencies of the stage were simulated using the modal analysis module of ANSYS. The first four modes are shown in Fig. 8(a)–(d). The first resonant mode is the out-of-plane mode along

Table 5
Cross-coupling between the axes of the nanopositioner.

Cross-Coupling (%)	X	Y	Z
X-axis Input	–	3.9	5.8
Y-axis Input	1.7	–	24

the Z-axis which appears at 249 Hz. The analytical model closely predicts this value with 255 Hz. To search for the lateral modes along the X and Y axes of the stage, the out-of-plane motions along the Z-axis were constrained. Fig. 8(e) and (f) show the lateral modes of the stage. The lateral resonance frequencies appear at 5243.3 Hz and 5225.2 Hz along the X and Y axes respectively, which are about 12% higher than the experimental results summarized in Table 6. The discrepancy is thought to be due to the soft boundary condition in the experimental system created by the adhesive mounting layer.

If higher out-of-plane resonance frequencies are required, the thickness can be increased. However, this will require proportionally higher actuation voltage, or multiple layers. Both options result in increased complexity and cost; however, these options may be desirable in applications where the out-of-plane resonance frequency should be maximized.

The harmonic response analysis module in ANSYS was used to simulate frequency responses of the stage. A damping ratio of 0.02 was applied to the model. A sinusoidal input within a bandwidth of 10 Hz to 6500 Hz was applied to the electrodes and the corresponding displacements of the central platform were recorded to construct the frequency responses shown in Fig. 11. FEA and experimental results are discussed in the next section.

6. Experimental characterization of the nanopositioner

This section presents the experimental identification and characterization of the sensitivity, range, cross-coupling, nonlinearity, and modal responses of the nanopositioner. Fig. 9 shows the experimental setup used to drive the piezoelectric bender actuators. A custom built amplifier with two input channels (V_x, V_y) and four output channels ($+V_x, -V_x, +V_y, -V_y$) provides the required voltages to actuate the device. To avoid de-polarization of the piezoelectric ceramic, the applied voltages are constrained to within ±200 V.

To characterize the sensitivity of each axis and the cross-coupling between axes, a single axis is driven with a 10 Hz sinusoidal voltage with the maximum 200 V amplitude. The resulting displacement of the nanopositioner, measured with an Attocube FPS3010 interferometer, is shown in Fig. 10(a–b). The peak-to-peak travel range was 10.08 μm in the X-axis and 10.45 μm in the Y-axis. The corresponding sensitivities of the X and Y axes are 25.2 nm/V and 26.1 nm/V respectively. These values are greater than the predicted values from the FEA of 18.6 nm/V and 18.1 nm/V. The discrepancy is attributed to the voltage dependence of the piezoelectric coefficient e_{31} which is measured under small signal conditions. With large signals, which are of interest in this work, the sensitivity of soft piezoceramics is known to increase by up to a factor of two [49].

The hysteresis of the stage is plotted in Fig. 10(c). The maximum difference between the upward and downward paths is 14% of the full-scale deflection, which is typical of PZT-5 A material. The stage also exhibits a creep of 13% after a period of 10 min, which is also typical of PZT-5A [50]. These non-linearities highlight the need for closed-loop control which will be addressed in future work.

The cross-coupling exhibited by the nanopositioner is listed in Table 5. There is significant cross-coupling between the X and Y axes, and the Z axis due to the low out-of-plane stiffness. However, it should be noted that the cross-coupling is highly linear and can therefore be effectively compensated by linear inversion methods, as demonstrated in [38]. In AFM applications, X→Y cross-coupling rotates the image, while the X→Z cross-coupling introduces a sloping plane artifact, both of which are routinely removed by image processing.

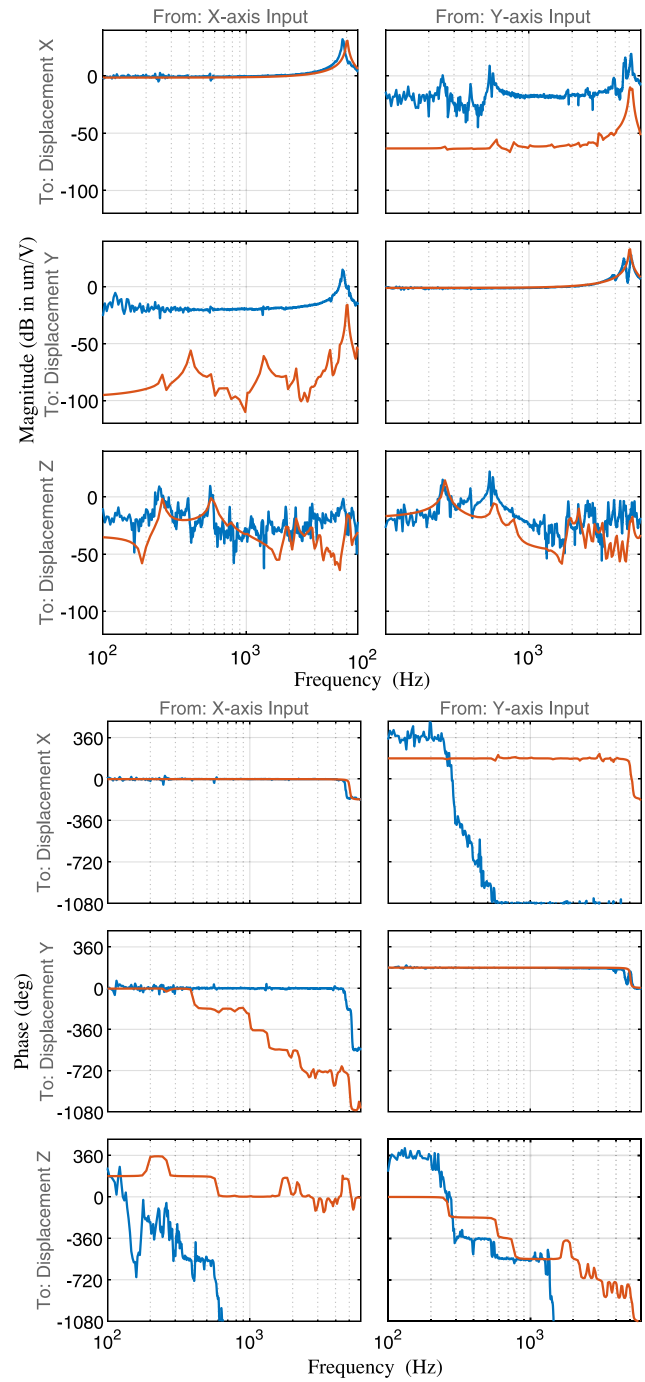

Fig. 11. The frequency responses of the stage. Experimental results are plotted in blue, FEA results are plotted in red. Experimental frequency responses are measured from the input applied to the voltage amplifiers, to the resulting displacements in the X, Y, and Z-axis. The amplifier voltage gain is 50. (For interpretation of the references to color in this figure legend, the reader is referred to the web version of this article.)

The frequency responses in Fig. 11 were measured with a Polytec MSA-100-3D laser vibrometer. The X and Y-axis resonances are observed near 5 kHz which agree with the FEA results. A number of resonances are observed in the Z-axis motion due to the low stiffness in this axis. The four large peaks with Y-axis excitation occur at 250 Hz,

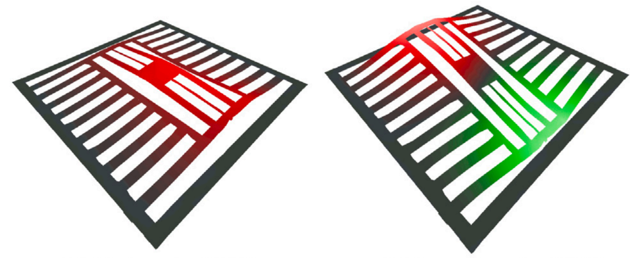

(a) First mode: 250 Hz (b) Second mode: 405 Hz

(c) Third mode: 556 Hz (d) Fourth mode: 570 Hz

Fig. 12. The measured mode shapes of the nanopositioner by exciting the outer Y-axis and measuring the motion over the entire piezoelectric structure with the Polytec MSA-100-3D laser vibrometer.

405 Hz, 556 Hz, and 570 Hz, which correspond to the four modes predicted by the FEA model. These four mode shapes are experimentally confirmed in Fig. 12 and are significantly larger with Y-axis actuation. A set of small low frequency modes are also observed in the Z-axis which are attributed to the resonance of the wires attached to the electrodes and the dynamics from the metal frame.

The experimental results for sensitivity and resonance frequency are compared to analytical and FEA predictions in Table 6.

The resolution of the nanopositioner can be measured directly [51] or predicted from the system noise processes [52]. In this work, the output noise density of the voltage amplifier is 1.25 $\mu V/\sqrt{Hz}$; therefore, the standard deviation of the positioning noise can be determined from the experimental frequency responses using Eq.3 in [51]. The standard deviation of the open-loop positioning noise is 9.0 nm in the X-axis, and 8.6 nm in the Y-axis. The slightly higher noise in the X-axis is due to the higher bandwidth in this axis. Improvements to the positioning resolution could be achieved by using a lower noise amplifier, or by using sensor-based feedback control to damp the resonances, which contribute strongly to the positioning noise [52].

7. AFM imaging

The proposed monolithic nanopositioning stage was used to scan a sample underneath a Nanosurf Atomic Force Microscope (AFM), as shown in Fig. 13. A 10 μm × 10 μm area of a BudgetSensors HS-100MG calibration grating was imaged in constant-force contact-mode with a resolution of 200 × 200 pixels. With the sample placed on the central platform of the nanopositioner, Fig. 14 (Left) shows an image captured using a 1 Hz scan rate. Image artifacts caused by hysteresis and cross-coupling can be observed.

An additional scan with a line-rate of 595 Hz is shown on the right of Fig. 14. This demonstrates a useful technique for high-speed AFM where a sinusoidal scan frequency is chosen at a minima of the X→Z response [6,53,54]. In this case, a minima is observed in Fig. 11 at approximately 600 Hz. When the sample is mounted on the stage, this frequency reduces to 595 Hz. A vibration-free image can be observed in Fig. 14 (right). The method is only applicable at a discrete set of frequencies where a zero in the response exists; however, it allows

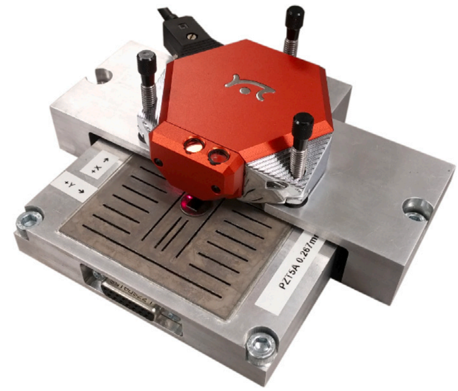

Fig. 13. The serial-kinematic stage used as an XY scanner mounted underneath a NanoSurf Atomic Force Microscope.

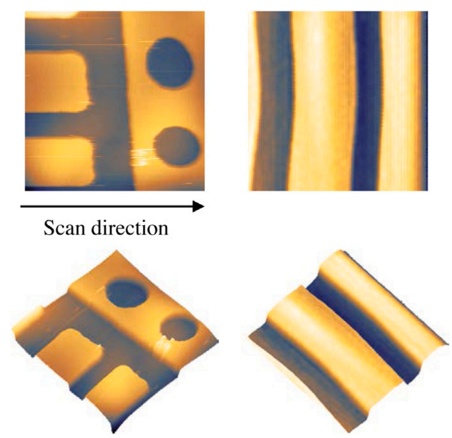

Fig. 14. AFM images of a calibration grating with a 5 μm pitch and 100 nm height. The top-down and orthographic images were obtained at 1-Hz line-rate (left column) and 595 Hz (right column).

Table 6
Comparison of characteristics of the nanopositioner from analytical, FEA, and experimental results.

	Analytical	FEA	Experimental
Inner X-axis gain (nm/V)	14.7	18.6	25.2
Outer Y-axis gain (nm/V)	15.2	18.1	26.1
X-axis resonance (Hz)	8321	5243	4690
Y-axis resonance (Hz)	8986	5225	4580
Z-axis resonance (Hz)	255	249	250

a much higher scan-rate than would normally be achievable from a system with a 250 Hz first resonance frequency.

Second, the scanning frequency was selected whereby the cross-coupling from the X to the Z axis is minimal. In Fig. 11, a zero in the X→Z frequency response is observed just above 600 Hz. When the sample is placed on the stage, the increased mass reduces this zero to 595 Hz and a scan is performed at this frequency. Fig. 14(right) shows an accurate, vibration free scan of a calibration grating using the 595 Hz scan rate which validates this approach. Image artifacts caused by non-linear hysteresis can be observed in the images.

8. Conclusions

This article describes the mechanics of a piezoelectric in-plane bender actuator. A serial-kinematic approach is then used to construct a dual-axis monolithic nanopositioning stage. Compared to previous monolithic nanopositioners that utilize extension actuators, the in-plane bender actuators offer a more flexible trade-off between deflection range and stiffness, and also eliminate push–pull actuation which has been associated with non-linear cross-coupling. However, compared to a parallel-kinematic stage of similar travel range, the serial kinematic design results in a lower vertical resonance frequency.

Future work includes increasing the stiffness in the out-of-plane direction by adding a vertical flexure, as described in [55]. This is expected to significantly increase the payload capacity and resonance frequency, but at the expense of increased height and more complex mechanical assembly. An alternative method for increasing the vertical stiffness is to increase the material thickness, which will require high actuation voltages or multiple layers. It is also intended to incorporate piezoresistive strain sensors or a three-axis capacitive sensor to enable active damping and reduction of cross-coupling and non-linearity [40, 56].

CRediT authorship contribution statement

Steven I. Moore: Methodology, Conceptualization, Formal analysis, Writing - original draft. **Yuen K. Yong:** Supervision, Conceptualization, Writing - review & editing. **Meysam Omidbeike:** Investigation, Validation, Writing - original draft. **Andrew J. Fleming:** Supervision, Conceptualization, Writing - review & editing.

Declaration of competing interest

The authors declare that they have no known competing financial interests or personal relationships that could have appeared to influence the work reported in this paper.

References

[1] Fleming AJ, Leang KK. Design, modeling and control of nanopositioning systems. London, UK: Springer; 2014.
[2] Rana MS, Pota HR, Petersen IR. Performance of sinusoidal scanning with MPC in AFM imaging. IEEE/ASME Trans Mechatronics 2015;20(1):73–83. http://dx.doi.org/10.1109/TMECH.2013.2295112.
[3] Bazaei A, Yong YK, Moheimani SR. Combining spiral scanning and internal model control for sequential AFM imaging at video rate. IEEE/ASME Trans Mechatronics 2016;22(1):371–80.
[4] Salapaka SM, Salapaka MV. Scanning probe microscopy. IEEE Control Syst 2008;28(2):65–83.
[5] Abramovitch DY, Andersson SB, Pao LY, Schitter G. A tutorial on the mechanisms, dynamics, and control of atomic force microscopes. In Proc. American control conference. New York City, NY; 2007, p. 3488–3502.
[6] Fleming AJ, Kenton BJ, Leang KK. Bridging the gap between conventional and video-speed scanning probe microscopes. Ultramicroscopy 2010;110(9):1205–14. http://dx.doi.org/10.1016/j.ultramic.2010.04.016.
[7] Fairbairn M, Moheimani SOR, Fleming AJ. Q control of an atomic force microscope micro-cantilever: a sensor-less approach. IEEE/ASME J Microelectromech Syst 2011;20(6):1372–81.
[8] Yong YK, Moheimani SOR. A compact XYZ scanner for fast atomic force microscopy in constant force contact mode. In IEEE/ASME international conference on advanced intelligent mechatronics. Montreal, Canada; 2010, p. 225–30.
[9] Sebastian A, Pantazi A, Pozidis H, Elefthriou E. Nanopositioning for probe-based data storage. IEEE Control Syst 2008;28(4):26–35.
[10] Mishra S, Coaplen J, Tomizuka M. Precision positioning of wafer scanners. Segmented iterative learning control for nonrepetitive disturbances. IEEE Control Syst 2007;27(4):20–5. http://dx.doi.org/10.1109/MCS.2007.384130.
[11] Ferreira A, Mavroidis C. Virtual reality and haptics for nanorobotics. IEEE Robot Autom Mag 2006;13(3):78–92.
[12] Fan Z-Q, Li X-W, Liu Y, Meng Q-G, Wang Y-P, Hou Y-P, et al. Piezo-assisted in vitro fertilization of mouse oocytes with spermatozoa retrieved from epididymides stored at 4 degree c. J Reprod Dev 2008;54(2):107–12.
[13] Hassen SZS, Heurs M, Huntington EH, Petersen IR, James MR. Frequency locking of an optical cavity using linear–quadratic Gaussian integral control. J Phys B: At Mol Opt Phys 2009;42(17):175501.
[14] Binnig G, Smith DPE. Single-tube three-dimensional scanner for scanning tunneling microscopy. Rev Sci Instrum 1986;57(8):1688–9.
[15] Maess J, Fleming AJ, Allgöwer F. Simulation of dynamics-coupling in piezoelectric tube scanners by reduced order finite element models. Rev Sci Instrum 2008;79:015105. http://dx.doi.org/10.1063/1.2826428, (1–9).
[16] Rana MS, Pota HR, Petersen IR. High-speed AFM image scanning using observer-based MPC-notch control. IEEE Trans Nanotechnol 2013;12(2):246–54.
[17] Cai K, Tian Y, Liu X, Fatikow S, Wang F, Cui L, et al. Modeling and controller design of a 6-DOF precision positioning system. Mech Syst Signal Process 2018;104:536–55.
[18] Chae KW, Kim W-B, Jeong YH. A transparent polymeric flexure-hinge nanopositioner, actuated by a piezoelectric stack actuator. Nanotechnology 2011;22(33):335501.
[19] Kenton BJ, Fleming AJ, Leang KK. A compact ultra-fast vertical nanopositioner for improving SPM scan speed. Rev Sci Instrum 2011;82(12):123703. http://dx.doi.org/10.1063/1.3664613, (1–8).
[20] Yong YK, Moheimani SOR, Kenton BJ, Leang KK. Invited review article: High-speed flexure-guided nanopositioning: Mechanical design and control issues. Rev Sci Instrum 2012;83(12):121101. http://dx.doi.org/10.1063/1.4765048.
[21] Liao C, Xu M, Xiao R, Han W. Integrated design of piezo-actuated 2-DOF submillimeter-range super-resolution platform with self-sensing unit. Mech Syst Signal Process 2020;139:106569.
[22] Kenton BJ, Leang KK. Design and control of a three-axis serial-kinematic high-bandwidth nanopositioner. IEEE/ASME Trans Mechatronics 2012;17(2):356–68.
[23] Yong YK, Moheimani SOR. Collocated Z-axis control of a high-speed nanopositioner for video-rate atomic force microscopy. IEEE Trans Nanotechnol 2015;14(2):338–45. http://dx.doi.org/10.1109/TNANO.2015.2394327.
[24] Ling M, Cao J, Jiang Z, Zeng M, Li Q. Optimal design of a piezo-actuated 2-DOF millimeter-range monolithic flexure mechanism with a pseudo-static model. Mech Syst Signal Process 2019;115:120–31.
[25] Liu P, Yan P, Özbay H. Design and trajectory tracking control of a piezoelectric nano-manipulator with actuator saturations. Mech Syst Signal Process 2018;111:529–44.
[26] Yong YK. A new preload mechanism for a high-speed piezoelectric stack nanopositioner. Mechatronics 2016;36:159–66. http://dx.doi.org/10.1016/j.mechatronics.2016.03.004.
[27] See Mad City Labs Inc., http://www.madcitylabs.com/nanolpseries.html on low-profile nanopositioners. [link]. URL http://www.madcitylabs.com/nanolpseries.html.
[28] See Kleindiek nanotechik, https://www.nanotechnik.com/sf-afm.html on Super-flat AFM system. [link]. URL https://www.nanotechnik.com/sf-afm.html.
[29] Zhou C, Gong Z, Chen BK, Cao Z, Yu J, Ru C, Tan M, Xie S, Sun Y. A closed-loop controlled nanomanipulation system for probing nanostructures inside scanning electron microscopes. IEEE/ASME Trans Mechatronics 2016;21(3):1233–41. http://dx.doi.org/10.1109/TMECH.2016.2533636.
[30] Zhang YL, Zhang Y, Ru C, Chen BK, Sun Y. A load-lock-compatible nanomanipulation system for scanning electron microscope. IEEE/ASME Trans Mechatronics 2013;18(1):230–7. http://dx.doi.org/10.1109/TMECH.2011.2166162.
[31] See Physik Instrumente on low-profile nanopositioners. [link]. URL https://www.physikinstrumente.com/en/products/nanopositioning-piezo-flexure-stages/xy-piezo-flexure-stages/p-5412-p-5422-xy-piezo-stage-201530/.
[32] Cao L, Liu H, Fu X, Zhang Z, Shen X, Ruan H. Comparison of UAV lidar and digital aerial photogrammetry point clouds for estimating forest structural attributes in subtropical planted forests. Forests 2019;10(2):145.
[33] Nikooienejad N, Maroufi M, Moheimani R. Iterative learning control for video-rate atomic force microscopy. IEEE/ASME Trans Mechatronics 2020.
[34] Mukhopadhyay D, Dong J, Ferreira PM. Parallel-kinematic-mechanism-based monolithic XY micropositioning stage with rotary comb drive actuators. In: Micromachining and microfabrication process technology XIII, Vol. 6882. International Society for Optics and Photonics; 2008, 688209.
[35] Alipour A, Coskun MB, Moheimani SR. A high bandwidth microelectromechanical system-based nanopositioner for scanning tunneling microscopy. Rev Sci Instrum 2019;90(7):073706.
[36] Rios S, Fleming AJ. A new electrical configuration for improving the range of piezoelectric bimorph benders. IEEE Trans Ultrason Ferroelectr Freq Control 2015;224:106–10. http://dx.doi.org/10.1016/j.sna.2015.01.031.
[37] Omidbeike M, Teo YR, Yong YK, Fleming AJ. Tracking control of a monolithic piezoelectric nanopositioning stage using an integrated sensor. In: IFAC world congress, Vol. 50. Toulouse, France: Elsevier BV; 2017, p. 10913–7. http://dx.doi.org/10.1016/j.ifacol.2017.08.2455.
[38] Omidbeike M, Eielsen AA, Yong YK, Fleming AJ. Multivariable model-less feedforward control of a monolithic nanopositioning stage with FIR filter inversion. In International conference on manipulation, automation and robotics at small scales. Helsinki, Finland; 2019.
[39] Omidbeike M, Yong YK, Moore SI, Fleming AJ. A five-axis monolithic nanopositioning stage constructed from a bimorph piezoelectric sheet. In International conference on manipulation, automation and robotics at small scales. Helsinki, Finland; 2019.
[40] Omidbeike M, Yong YK, Fleming AJ. Sensing and decentralized control of a five-axis monolithic nanopositioning stage. In: IFAC world congress. 2020.
[41] Fleming A, Yong YK. An ultra-thin monolithic XY nanopositioning stage constructed from a single sheet of piezoelectric material. IEEE/ASME Trans Mechatronics 2017;22(6):2611–8. http://dx.doi.org/10.1109/TMECH.2017.2755659.
[42] Moore S, Omidbeike M, Fleming AJ, Yong YK. A monolithic serial-kinematic nanopositioner with integrated sensors and actuators. In IEEE international conference on advanced intelligent mechatronics. Auckland, New Zealand; 2018.

[43] Cowper GR. The shear coefficient in timoshenko's beam theory. J Appl Mech 1966;33(2):335–40. http://dx.doi.org/10.1115/1.3625046.
[44] Piefort V. Finite element modelling of piezoelectric active structures (Ph.D. thesis), Universite Libre de Bruxelles; 2001.
[45] Reddy JN. Energy principles and variational methods in applied mechanics. John Wiley & Sons; 2002.
[46] Inman D. Engineering vibration. Pearson; 2014.
[47] Quek S, Liu G. Finite element method: A practical course. Elsevier Science; 2003, URL https://books.google.com.au/books?id=_xbugmEwQz8C.
[48] Han SM, Benaroya H, Wei T. Dynamics of transversely vibrating beams using four engineering theories. J Sound Vib 1999;225(5):935–88.
[49] Pacheco M, Santoyo FM, Méndez A, Zenteno L. Piezoelectric-modulated optical fibre bragg grating high-voltage sensor. Meas Sci Technol 1999;10(9):777.
[50] Pota H, Petersen IR, Rana M, et al. Creep, hysteresis, and cross-coupling reduction in the high-precision positioning of the piezoelectric scanner stage of an atomic force microscope. IEEE Trans Nanotechnol 2013;12(6):1125–34.
[51] Fleming AJ. Note: A method for estimating the resolution of nanopositioning systems. Rev Sci Instrum 2012;83(8):086101.
[52] Fleming AJ. Measuring and predicting resolution in nanopositioning systems. Mechatronics 2014;24(6):605–18.
[53] Teo YR, Yong YK, Fleming AJ. A comparison of scanning methods and the vertical control implications for scanning probe microscopy. Asian J Control 2017;19(2):1–15. http://dx.doi.org/10.1002/asjc.1422.
[54] Humphris ADL, Miles MJ, Hobbs JK. A mechanical microscope: High-speed atomic force microscopy. Appl Phys Lett 2005;86(3):034106. http://dx.doi.org/10.1063/1.1855407.
[55] Hao G, Kong X. A novel large-range XY compliant parallel manipulator with enhanced out-of-plane stiffness. J Mech Des 2012;134(6):061009.
[56] Dong J, Salapaka SM, Ferreira PM. Robust control of a parallel-kinematic nanopositioner. J Dyn Syst Meas Control 2008;130(4).

Steven Ian Moore graduated from the University of Newcastle, Australia with a Bachelor of Electrical Engineering and a Bachelor of Mathematics in 2012, and a PhD degree in electrical engineering in 2016. He is currently a post-doctoral researcher with the Precision Mechatronics Lab at the University of Newcastle. His research focus is on the design, modeling, implementation, and optimization of mechatronic systems including precision motion control and sensing in Microelectromechanical systems (MEMS), structural design of piezoelectric micro-cantilevers, nanopositioning, ultra-high bandwidth fixed point control realizations, image stabilization in optical systems, and inertial stabilization systems.

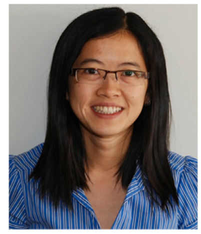

Yuen Kuan Yong received the Bachelor of Engineering degree in Mechatronics Engineering and the PhD degree in mechanical engineering from The University of Adelaide, Australia, in 2001 and 2007, respectively. She was an Australian Research Council DECRA Fellow from 2013 to 2017. She is currently an associate professor with the School of Electrical Engineering and Computing, The University of Newcastle, Australia. Her research interests include nanopositioning systems, design and control of novel micro-cantilevers, atomic force microscopy, and miniature robotics. A/Prof Yong is the recipient of the University of Newcastle Vice-Chancellor's Award for Research Excellence in 2014, and the Vice-Chancellor's Award for Research Supervision Excellence in 2017. She is an associate editor for the IEEE/ASME Transactions of Mechatronics.

Meysam Omidbeike graduated from the University of Newcastle, Australia with a Bachelor of Electrical Engineering in 2015. He is currently a PhD student within the Precision Mechatronics Lab, located in the School of Electrical Engineering and Computer Science, The University of Newcastle. His research focus is on design, sensing and control of monolithic piezoelectric devices including nanopositioning, multivariable precision sensing and control, sensor fusion, digital signal processing and vibration control.

Andrew J. Fleming graduated from The University of Newcastle, Australia (Callaghan campus) with a Bachelor of Electrical Engineering in 2000 and PhD in 2004. Prof Fleming is the Director of the Precision Mechatronics Lab at The University of Newcastle, Australia. His research interests include lithography, nano-positioning, scanning probe microscopy, and biomedical devices. Prof Fleming's research awards include the ATSE Baterham Medal in 2016, the IEEE Control Systems Society Outstanding Paper Award in 2007, and The University of Newcastle Researcher of the Year Award in 2007. He is the co-author of three books and more than 180 Journal and Conference articles. Prof Fleming is the inventor of several patent applications, and in 2012 he received the Newcastle Innovation Rising Star Award for Excellence in Industrial Engagement.